International Journal of Machine Tools & Manufacture 176 (2022) 103887

Contents lists available at ScienceDirect

International Journal of Machine Tools and Manufacture

journal homepage: www.elsevier.com/locate/ijmactool

Sinter formation during directed energy deposition of titanium alloy powders

Lorna Sinclair [a,b,**], Samuel J. Clark [a,b], Yunhui Chen [a,b,c], Sebastian Marussi [a,b], Saurabh Shah [a,b], Oxana V. Magdysyuk [d], Robert C. Atwood [d], Gavin J. Baxter [e,f], Martyn Jones [e], D. Graham McCartney [g], Chu Lun Alex Leung [a,b], Peter D. Lee [a,b,*]

[a] Department of Mechanical Engineering, University College London, WC1E 7JE, UK
[b] Research Complex at Harwell, Rutherford Appleton Laboratory, Harwell, Didcot, OX11 0FA, UK
[c] X-ray Science Division, Argonne National Laboratory, Lemont, IL, 60439, USA
[d] Diamond Light Source Ltd, Harwell Campus, Didcot, OX11 0DE, UK
[e] Rolls-Royce Plc, PO Box 31, Derby, Derbyshire, DE24 8BJ, UK
[f] Department of Materials Science and Engineering, University of Sheffield, Mappin St, Sheffield, S1 3JD, UK
[g] Faculty of Engineering, University of Nottingham, University Park Nottingham, NG7 2RD, UK

ARTICLE INFO

Keywords:
Laser additive manufacturing
Directed energy deposition
Synchrotron X-ray imaging
Sintering
Porosity formation

ABSTRACT

During directed energy deposition (DED) additive manufacturing, powder agglomeration and sintering can occur outside of the melt pool when using titanium alloy powders. Using *in situ* synchrotron radiography we investigate the mechanisms by which sintering of Ti6242 powder occurs around the pool, performing a parametric study to determine the influence of laser power and stage traverse speed on sinter build-up. The results reveal that detrimental sinter can be reduced using a high laser power or increased stage traverse speed, although the latter also reduces deposition layer thickness. The mechanism of sinter formation during DED was determined to be in-flight heating of the powder particles in the laser beam. Calculations of particle heating under the processing conditions explored in this study confirm that powder particles can reasonably exceed 700 °C, the threshold for Ti surface oxide dissolution, and thus the powder is prone to sintering if not incorporated into the melt pool. The build-up of sinter powder layer on deposit surfaces led to lack of fusion pores. To mitigate sinter formation and its detrimental effects on DED component quality, it is essential that the powder delivery spot area is smaller than the melt pool, ensuring most powder lands in the melt pool.

1. Introduction

Laser Directed Energy Deposition (DED) is an additive manufacture (AM) is a fabrication technique for the rapid production of complex components by progressively adding layers of material via simultaneous delivery of laser energy with either wire or powder as feedstock [1]. It is particularly useful for producing large free-form parts, adding surface coatings [2], joining dissimilar materials [3], building functionally graded components [4], or for use in repair applications [5,6]. The elimination of porosity in DED builds presents one of the greatest challenges: porosity can be a result of entrapped gas in the feedstock powder [7], entrained shield [8] or carrier gas [9], or lack of fusion pores caused by insufficient melting between deposition layers [1].

Many DED studies have concentrated on exploring the relationships between DED nozzle geometries and the powder deposition characteristics, including interactions between the powder jet and the laser beam or the nozzle working distance [10]. Laser attenuation increases is affected by processing conditions and powder focus, increasing powder feed rate [11], and the work by Pinkerton et al. [12] has shown that in-flight powder heating varies across the width a laser beam. Tan et al. [13] reported the divergence of powder jets over prolonged powder feeding times, which decreased deposit height due to reduced powder capture.

Wolff et al. [14] conducted *in situ* synchrotron X-ray imaging of powder DED using a process replicator with a piezo-driven system to deliver powder to a laser spot, in which high speed radiography

* Corresponding author. Department of Mechanical Engineering, University College London, WC1E 7JE, UK.
** Corresponding author. Department of Mechanical Engineering, University College London, WC1E 7JE, UK.
E-mail addresses: lorna.sinclair.18@ucl.ac.uk (L. Sinclair), peter.lee@ucl.ac.uk (P.D. Lee).

https://doi.org/10.1016/j.ijmachtools.2022.103887
Received 30 November 2021; Received in revised form 10 April 2022; Accepted 11 April 2022
Available online 29 April 2022

provided important new insights into melt pool formation, gravitational powder flow, and the powder capture into a melt pool. *In situ* work on melt pool geometry [15,16] and porosity formation mechanisms in DED has also been carried out [17]. However, the conditions used in these studies involved a much smaller spot size and lower powder feed rate compared to industrial DED processes, as it was optimised for high resolution and high-speed imaging of powder. Chen et al. performed *in situ* synchrotron X-ray radiographic characterisation studies using a blown powder process replicator (BAMPR) that more closely emulates the characteristics of an industrial system. Varying laser power, speed, and powder feedrate in DED of austenitic grade 316 L stainless steel (SS316L) revealed changes to melt pool geometries and surface roughness [18]. Furthermore, examination of the nickel-based superalloy IN718 [19] and the industrially important titanium alloy Ti6242 (Ti–6Al–2Sn–4Zr–2Mo in wt%) [20] has revealed mechanisms of track development and porosity formation during DED, highlighting substantial differences in the melt pool shapes of these alloys under the conditions investigated.

Fig. 1 summarises these differences, observed using *in situ* synchrotron X-ray imaging of 3 different materials: **(a)** SS316L**; (b)** IN718; and **(c)** Ti6242, *after* [18,19]. SS316L and IN718 exhibit a uniform track with some partially-melted powder particles visible on the solidified track surface as shown by the blue arrows. In the case of Ti6242 (Fig. 1c), a large amount of powder is visible, which appears to have accumulated on the track surface in a layer *ca.* 300 μm thick. Chen et al. [20] proposed that powder sintering was responsible for this powder build up. Nickel and steel alloys both form stable Cr-based oxides [21,22], which inhibit sintering, whereas titanium oxide films can diffuse into the bulk as interstitial oxygen at temperatures well below the melting point [23]. In our previous DED studies on SS316L [18] and IN718 [19], powder agglomeration around the melt pool was not visible for the conditions tested, across a range of laser powers, traverse speeds, or powder feedrates. A range of other processing conditions for SS316L and IN718 are shown in Supplementary Figs. 1, 2 respectively.

Henceforth in this work, *powder agglomeration* and *sinter* refer to the accumulation of unmelted powder particles, which are bonded together via necking, reminiscent of early stage sintering. Unmelted powder particles adhering to the track has been reported for SS316L and attributed to misalignment of the laser beam or the powder spot [24]. Syed et al. [25] indicated three explanations for powder adhering to track surfaces: particles heated in the laser loosely adhering to the solidified track; solid particles impacting the end of the melt pool, with insufficient heat to fully melt and incorporate them; or particles which impact the melt pool and become semi-molten. However, the number or semi-melted particles is significantly less than that seen with Ti alloys. Gharbi et al. [26] observed excessive powder agglomeration on the surface of Ti–6Al–4V tracks during DED.

The agglomerated Ti powder layer has a profound effect on the advancing melt pool. It significantly alters the pool shape (forming a concave rather than convex surface), appears to alter the wetting angle at the front of the melt pool, and will thus lead to markedly different multilayer build characteristics between the three materials. Supplementary Table 1 and Supplementary Fig. 3 show a comparison of typical DED processing conditions for titanium alloys.

The aim of the work is to use *in situ* synchrotron X-ray imaging to further explore the influence of the DED process conditions on titanium and titanium alloy powder deposition during multi-layer builds. Specifically, this paper will investigate the hypothesis that sintering is the mechanism causing powder accumulation on the surface and explore how this can be mitigated, reducing a potential cause of defects such as lack of fusion porosity.

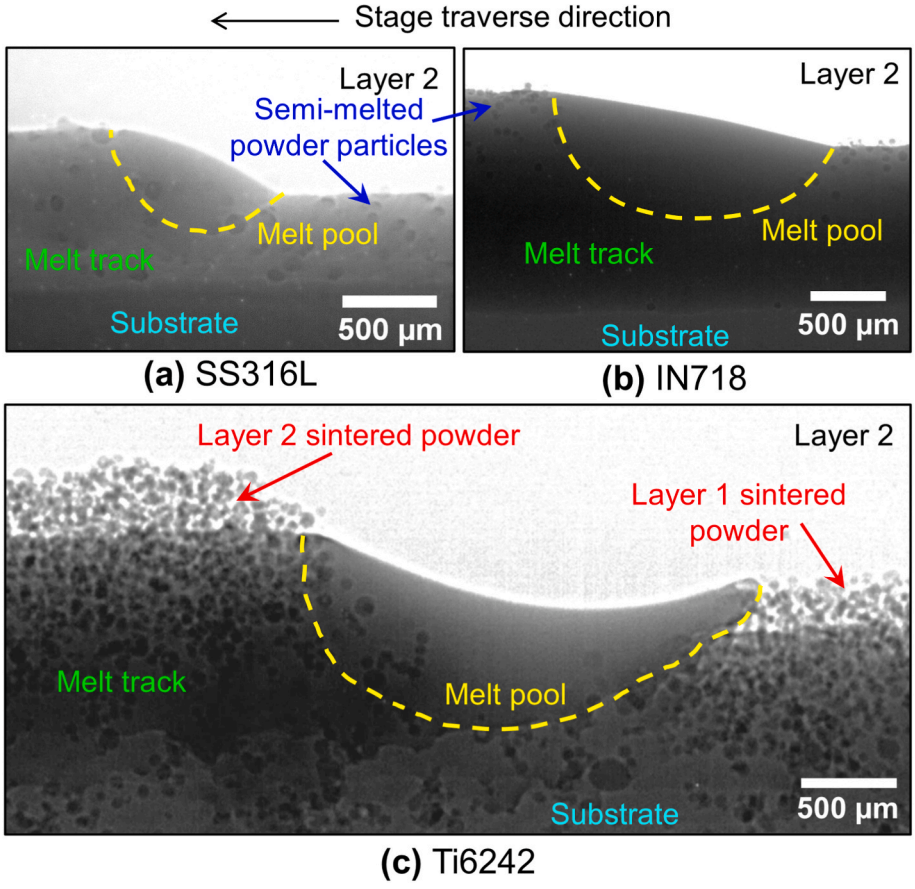

Fig. 1. *In situ* synchrotron X-ray images of (a) SS316L, (b) IN718 and (c) Ti6242 DED multilayer builds using BAMPR at laser power 200 W, stage traverse speed 1 mm s^{-1}. The melt pool shape boundary is shown by the dashed yellow line. The blue arrows indicate semi-melted powder particles adhered to the track surface, and red arrows indicate additional sintered powder not incorporated into the melt pool. Significant differences are seen in both the melt pool shape and the deposition of powder on the track surface, after [18,19]. (For interpretation of the references to colour in this figure legend, the reader is referred to the Web version of this article.)

2. Experimental methods

2.1. Materials

Two gas atomised powders were used in this study: Ti6242 (Ti–6Al–2Sn–4Zr–2Mo in wt%), and Commercially Pure (CP) Ti (both from *Carpenter Additive, UK*). The Ti6242 powder had a nominal size range of 45–106 μm with $D_{10} = 50$ μm, $D_{50} = 74$ μm, and $D_{90} = 90$ μm. The substrates were made from Ti6246 (Ti–6Al–2Sn–4Zr–6Mo in wt%) and CP Ti for the alloy and CP Ti powders, respectively. Substrates were 1 mm thick to allow for adequate X-ray transmission during imaging and to emulate thin wall builds by aiming to keep conductive heat losses approximately the same in all layers.

The primary investigation used Ti6242 powder, and a limited number of additional experiments were conducted using CP Ti powder and substrates. This was to determine whether the observed sintering effect is a specific feature of Ti6242 or is a more general phenomenon that occurs during DED of titanium-based powders.

2.2. In situ blown powder DED process replicator

A laser blown powder DED additive manufacturing process replicator (BAMPR) was designed to replicate a commercial laser blown powder DED system, with the ability to be employed onto a synchrotron beamline. The system is described in detail in previous works [19]. Briefly, the system is composed of an industrial DED nozzle and a 200 W continuous wave 1070 nm Yb-doped fibre laser (SPI Lasers Ltd, UK). The laser was focussed to a 400 μm ($4\sigma_{xy}$) diameter spot using tuneable optics (Optogama, Lithuania) and was aligned along the nozzle axis. The laser beam had a Gaussian distribution [27]. Powder delivery was via four jets arranged concentrically with the nozzle axis. An industrial powder feeder (Oerlikon Metco TWIN-10-C, Germany) was used to deliver powder to the nozzle via argon gas flow, at a constant flowrate. An additional argon shield gas flowed axially through the nozzle to create an inert atmosphere around the laser melting area and prevent oxidation. The substrates onto which powder was deposited were mounted onto a 3-axis *XYZ* motion stage (Aerotech Inc, USA) with travel of 25 × 50 × 50 mm (length × width × height). The entire deposition system was enclosed in an environmental chamber with X-ray transparent Kapton film windows. The chamber was evacuated and backfilled with argon (99.998% purity) prior to powder deposition.

2.3. Experimental build conditions

A range of processing parameters were investigated to observe the effect of laser power and sample traverse speed during DED, as shown in Table 1. Each build was a single track, 8 mm long in the *x*-direction. The stage was lowered in the *z*-direction for each deposition layer to maintain a consistent working distance between the nozzle and the sample. Samples built at 200 W were 5 layers high (*z*-direction), and samples at 150 W and 100 W were built 4 layers high. The final layer was not deposited for the latter conditions, as the emerging sinter layer approached the nozzle and posed a powder blockage risk. Layers were added in a bi-directional scanning strategy, alternating each layer. This choice of processing parameters was a compromise between replicating industrial conditions as accurately as possible whilst maintaining optimum imaging requirements.

Table 1
Processing parameters selected for Ti6242 builds.

Experimental condition	Laser power, *P* (W)	Traverse speed, *v* (mm s^{-1})	Powder feedrate, *f* (g min^{-1})
1	100	1	1
2	150	1	1
3	200	1	1
4	200	2.5	1
5	200	5	1

2.4. In situ synchrotron radiography

In situ X-ray radiography experiments were carried out at the I12 Joint Engineering, Environmental and Processing (JEEP) beamline at Diamond Light Source (UK) [28]. A monochromatic X-ray beam was used with a mean energy of 53 keV. The imaging system consisted of a LuAg:Ce scintillator and a 2x magnification long working distance objective lens (0.21 numerical aperture). The radiograph images were captured using a PCO. edge high-resolution imaging camera (PCO, Germany) at 200 frames per second, with an exposure time of 4 ms and an effective pixel size of *ca.* 3.24 μm. The framerate of 200 fps was selected as the optimal compromise for beamline I12 between sufficient temporal resolution and X-ray transmission for image signal to noise ratio, and high spatial resolution. This combination of frame rate and spatial resolution was appropriate to capture the powder agglomeration and its interaction with the melt pool as well as the formation of lack of fusion pores.

2.5. Characterisation and micro-computed tomography (μCT)

The samples were examined by scanning electron microscopy (SEM) in secondary electron imaging mode at 10 kV (JEOL JSM-6610 LV, Tokyo). Images were taken of the top surface of the track after the final deposition layer.

Multilayer samples were also examined *ex situ* by micro-computed tomography (μCT) using a Phoenix Nanotom (General Electric, USA) to image and quantify microstructural features such as porosity. 1000 projections were collected over 360°, with an exposure time of 1 s. The data were reconstructed using filtered back projection [29], resulting in a voxel edge size of 8 μm [30]. The image analysis was performed using Avizo 9.3 (ThermoFisher Scientific) [31].

2.6. Image analysis of synchrotron radiographs

The open-source software Fiji version 1.52i [32] was used to analyse radiographs. Flat-field correction removed artefacts and noise variation inherited during the acquisition process; 100 flat-field and 100 dark-field X-ray images were collected to do so. The acquired radiographs were normalised using the standard flat-field correction (FFC) equation [27].

After FFC, measurements were taken from the radiograph images. The deposition height was measured as the thickness of the added material onto the previous layer build height; not including any remelt depth in the measurement. The sinter height was measured as the thickness of the powder particles visible above the solid material for each layer. The measurements are shown graphically in Supplementary Fig. 4.

3. Results

The results show a large amount of Ti6242 powder on the track surface following a 5-layer build for a range of laser powers and speeds. Left to right in Fig. 2a-e, the track widths (*y*-direction) were 2.2 mm, 2.1 mm, 2.8 mm, 1.0 mm, and 1.2 mm respectively. The amount of sintered powder visible on the surface decreases with an increase in traverse speed. Fig. 2f highlights the sintering in Fig. 2a, with sintered powder denoted by pink dashed arrows, and semi-fused powder by yellow arrows. Fig. 2g shows a high magnification image of powder particles, displaying sinter necking. The necks between particles in Fig. 2f and g are 19 ± 3 μm in length. Although Fig. 2 illustrates the presence of both semi-melted and sintered powder particles on the track surface, the amount of semi-melted particles is low compared to sintered particles, and hereafter the large accumulation of powder will be referred to as a

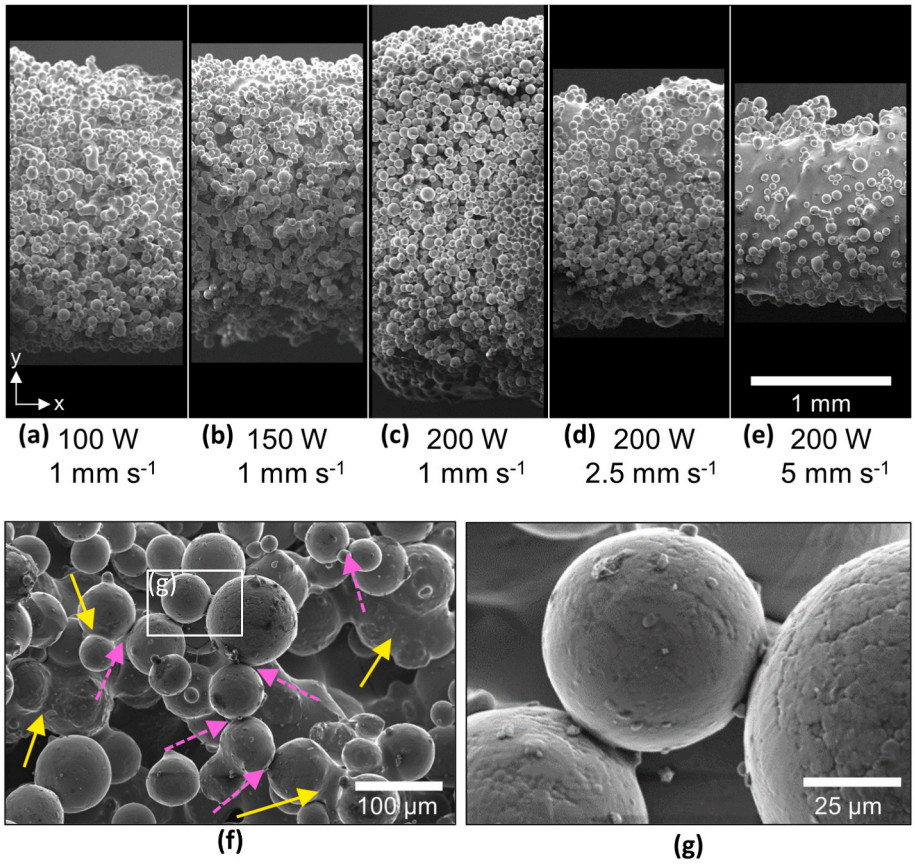

Fig. 2. Secondary electron SEM images of Ti6242 powder accumulated on the surface of tracks following 5 layers of *in situ* DED. (a–e) Low magnification images of the top surface showing accumulation at each processing condition. (f) Higher magnification images of powder particles on the surface of the (a), showing some that appear sintered (pink dashed arrows), and others semi-melted and fused together (yellow arrows). (g) Example of particles that exhibit sintering. (For interpretation of the references to colour in this figure legend, the reader is referred to the Web version of this article.)

sintered powder layer. Images of powder sintering for the conditions in Fig. 2b–e are shown in Supplementary Fig. 5a–d.

Reconstructed µCT images of the tracks are shown in Fig. 3. There is a large decrease in interlayer porosity between deposition layers as the laser power increases from 100 W to 200 W. At the 1 mm s^{-1} and 100 W deposition condition, a considerable amount of sintered powder is visible, with a thick layer on the top surface. Layers were not fused together, and there is unmelted powder visible between layers, forming interlayer pores. The cross section shows no layer cohesion. The track detached from the substrate during µCT sample preparation due to insufficient fusion of the melt track to the substrate during layer 1 deposition. The 150 W condition reveals large, interconnected interlayer pores between layers. Sintered powder can be seen between melt layers on the sides and top surface of the track. The 200 W condition induced sintered powder on the outside of the track, and the cross section shows an inverted 'saddle' shaped melt pool [20], increasing in width as the layer number increased. Some smaller pores were visible at layer boundaries, as well as small spherical pores at the end of the track. As traverse speed increased to 2.5 mm s^{-1}, the layer thickness decreased, but the width of the track similarly increased with each deposited layer. Much less sinter is present on the track surface; however, some particles can be seen along the sides of the track. At $v = 5$ mm s^{-1}, the layer thickness is smaller, and some lack of fusion pores can be seen between the substrate and layer 1. Since sintered powder on the track surfaces can be seen in Fig. 2, it is possible that sintered particles were inadvertently removed from the samples during preparation for µCT, as the sintered particles were not strongly bonded to the track surface. The percentage volume of lack of fusion porosity between build layers caused by the sintered powder particles, if the whole sample were to be considered as a solid track, is listed in Table 2.

In situ synchrotron X-ray images obtained during the building process are shown in Fig. 4 and Supplementary Videos 1–4, where the effects of laser power on the formation of accumulated powder layers are revealed. Fig. 4a shows layer 1 melting at 100 W. The melt track shows insufficient wetting to the substrate, and a layer of sintered powder on the track surface *ca.* 650 µm thick; roughly twice as thick as the melt track itself. The powder delivery gave a focussed powder footprint from all four incoming jets of 4.9 ± 0.1 mm diameter. Therefore, despite the centre of the powder jet impinging on the laser spot, a large fraction of the powder jet is not striking the melt pool due to its relatively small size. The deposition of layer 3 at the same condition is in Fig. 4b, in which the thick powder layer has created a barrier between the solidified layer 2 melt track, and the melt pool, resulting in lack of fusion defects between layers. The melt pool is considerably longer than for layer 1. Fig. 4c shows layer 1 melting at a laser power of 200 W. A deep hemispherical melt pool remelting the substrate, and a layer of sintered powder on top of the melt track, *ca.* 300 µm thick, are both evident. A cluster of sintered powder ahead of the melt pool is also visible, which was later incorporated into the melt pool as seen in Supplementary Video 3. In this case, the larger melt pool would increase the powder capture efficiency compared to the 100 W condition. Fig. 4d shows layer 3 of the same 200 W laser power condition, showing an elongated melt pool, and a change in wetting at the front of the melt pool, caused by the layer of sintered powder pre-existing track. In this case, the melt pool was large enough to ensure sufficient fusion between layers.

Fig. 5 and Supplementary Videos 5–8 demonstrate the effect of transverse speed on the formation of sintered powder layers. For comparison, the 1 mm s^{-1} processing condition is in Fig. 4c, d. Fig. 5a shows layer 1 melting at 2.5 mm s^{-1} showing a smaller melt pool, and reduced sinter layer compared to the 1 mms^{-1} traverse speed. However, the melt pool still remelts the substrate sufficiently to achieve bonding. The deposited layer height in this case is 260 ± 11 µm. Fig. 5b is layer 3 melting for the same condition, showing an elongated melt pool and reduced melt pool depth. The change in wetting at the front of the melt

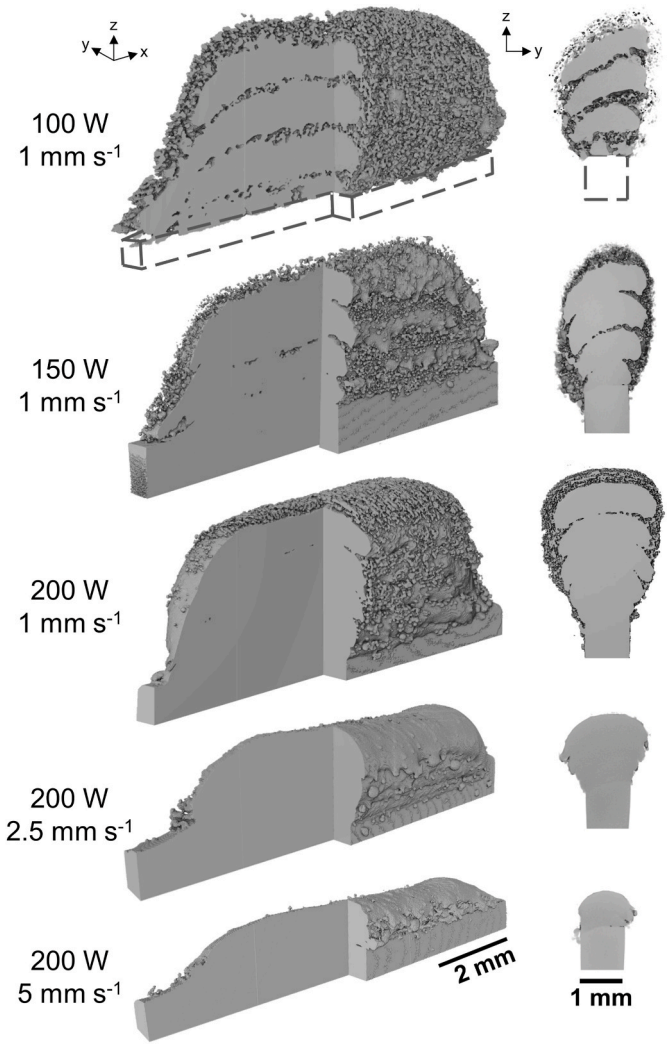

Fig. 3. µCT rendered images of tracks with a quarter section removed, and cross sections, showing track widening and lack of fusion between layers. The 100 W condition detached from the substrate during sample preparation due to insufficient melting in layer 1 deposition (shown in Fig. 4), and so the approximate substrate size is drawn in dotted lines.

pool caused by the sinter layer is also observed here. Fig. 5c shows layer 1 melting for a traverse speed of 5 mm s^{-1}. The melt pool is smaller with a deposited track height of 145 ± 9 µm. Fig. 5d is layer 3 melting, similarly showing an elongated and shallower melt pool than layer 1.

Table 2 includes the average deposited layer thickness measurements for all conditions: the 100 W and 150 W conditions show a high deposited layer thickness because the sinter layer prevents complete fusion to take place and the deposited track is built upon the sintered layer.

The measurements of the sintered layer height for each processing condition are summarised in Fig. 6, as described in Supplementary Fig. 4, averaged over all deposition layers. The 200 W, 1 mm s^{-1} condition is plotted on both graphs. Inset radiograph images show a visual representation of the changing sinter height for each process condition. Fig. 6a shows that changing laser power has a significant effect on the height of the sintered layer, as decreasing from 200 W to 100 W increased the sinter height by *ca.* 400 µm. Fig. 6b shows that increasing the stage traverse speed decreases the sintered layer height: increasing from 1 to 5 mm s^{-1} decreased the sinter layer by *ca.* 130 µm. This is likely due to less powder being deposited during the total build time, as it takes 1/5 of the time to deposit each layer, and thus there is 80% less powder delivered per track length at a constant powder feedrate.

A limited number of experiments were conducted using CP Ti powder and substrates. Radiographic results are shown in Fig. 7, built at 200 W, 2.5 mm s^{-1}, and powder feedrate of 1 g min^{-1}. Supplementary Video 9 shows the deposition at 5 mm s^{-1}, similarly showing a reduced sinter layer height, demonstrating that the relationship between the formation of sinter layer and the processing parameters is probably common across Ti-based materials. Fig. 7b shows sintered CP Ti powder particles on the track surface. The CP Ti behaves similarly to the Ti6242 (Fig. 2); most of the powder particles are sintered together rather than semi-melted and fused to the track. This data shows that the powder sintering phenomenon is not unique to Ti6242 powder and may affect other Ti alloys as well.

4. Discussion

In this study, we observed that Ti alloy powder accumulates on the track surface behind the pool during deposition. The SEM images show only a small fraction of powder particles appear partially-melted and fused together and the majority of the powder particles appear to be sintered. The evidence for this is shown in Fig. 2f, as some particles are most likely partially-melted and fused together, as they have changed in shape, whereas the majority of particles resemble that of Fig. 2g, having developed a neck feature between particles. This feature does not distort the particles and they retain a spherical shape, indicating early stage sintering [33]. Powder build-up via other means such as high velocity impacts, analogous to the cold-spray technique, was ruled out as a mechanism for sinter formation, as the powder particles shown in Fig. 2 have no obvious signs of impact deformation. Schmidt et al. have performed extensive work on determining the critical impact velocity for the cold spray process, which for titanium was predicted and measured to be in excess of 700 m s^{-1} [34]. In DED it could be argued that the highly elevated temperature of some particles would cause the critical impact velocity to be much lower, due to higher ductility. Goldbaum et al. show that even in the cases of gas heated to 1000 °C, the critical velocity remains in excess of 400 m s^{-1} [35], approximately 15 times the maximum velocity of particles exiting our DED nozzle.

The sinter layer formed during deposition is a feature of the experimental setup, and the thermal properties of the powder. Due to the rapid processing times, high heat input in DED, and accelerated diffusion at these high temperatures [36], it is speculated that solid state sintering or even liquid phase sintering is responsible for powder agglomeration [20]. For Ti, furnace sintering generally occurs in the

Table 2
Melt pool measurements and estimated melt pool area in the final deposition layer for each processing condition, average sinter height and deposited layer thickness measurements across all layers, the percentage volume of lack of fusion porosity between deposition layers caused by sintered particles, and the powder capture efficiency.

P	*v*	Melt pool width (mm)	Melt pool length (mm)	Ellipse melt pool area (mm^2)	Ratio of pool area to powder spot (%)	Average sinter height (mm)	Average deposited layer thickness (mm)	Lack of fusion porosity (%)	Powder capture efficiency (%)
100	1	2.17 ± 0.07	1.51 ± 0.05	2.58	13.7	0.68 ± 0.10	0.57 ± 0.15	29.6	8.4
150	1	2.06 ± 0.04	1.81 ± 0.04	2.93	15.5	0.53 ± 0.11	0.67 ± 0.11	13.1	9.3
200	1	2.77 ± 0.04	2.30 ± 0.02	5.01	26.6	0.30 ± 0.07	0.60 ± 0.08	9.3	10.1
200	2.5	1.75 ± 0.05	2.01 ± 0.09	2.77	14.7	0.21 ± 0.04	0.31 ± 0.03	3.0	8.4
200	5	1.24 ± 0.04	1.65 ± 0.07	1.61	8.5	0.17 ± 0.03	0.19 ± 0.05	3.7	5.5

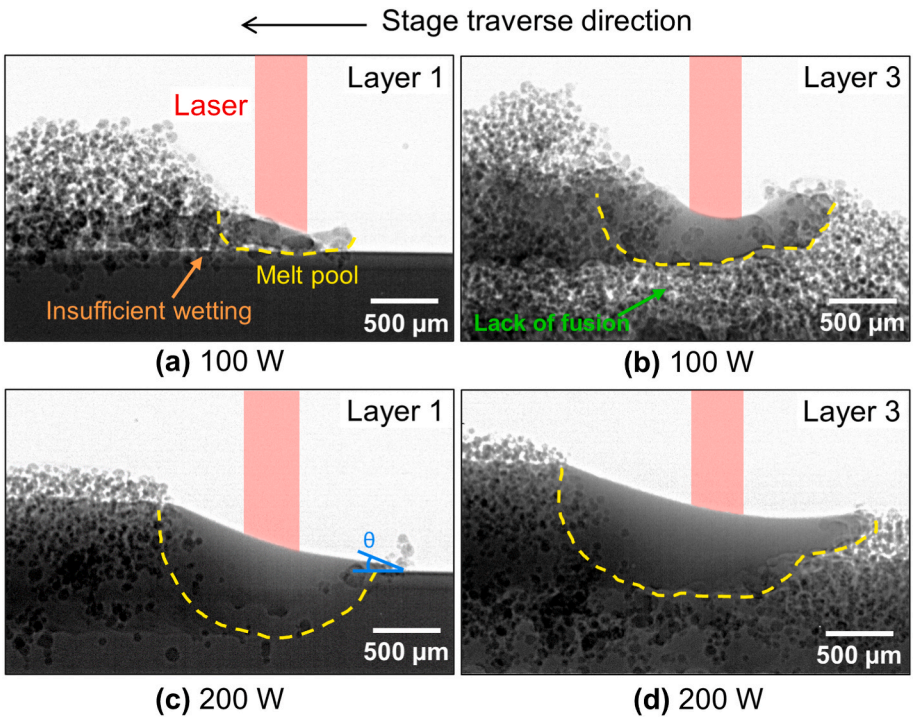

Fig. 4. Effect of laser power on agglomerated powder height, with (a–b) at 100 W, and (c–d) at 200 W, for $v = 1$ mm s^{-1} and $f = 1$ g min^{-1}. The approximate laser beam position is shown in red. The powder spot diameter at the substrate is ca. 4.9 ± 0.1 mm. (a) Radiograph of layer 1 deposition at 100 W. (b) Layer 3 deposition. (c) Layer 1 deposition at 200 W, with the advancing wetting angle, θ, shown in blue. (d) Layer 3 deposition. See Supplementary Videos 1–4. (For interpretation of the references to colour in this figure legend, the reader is referred to the Web version of this article.)

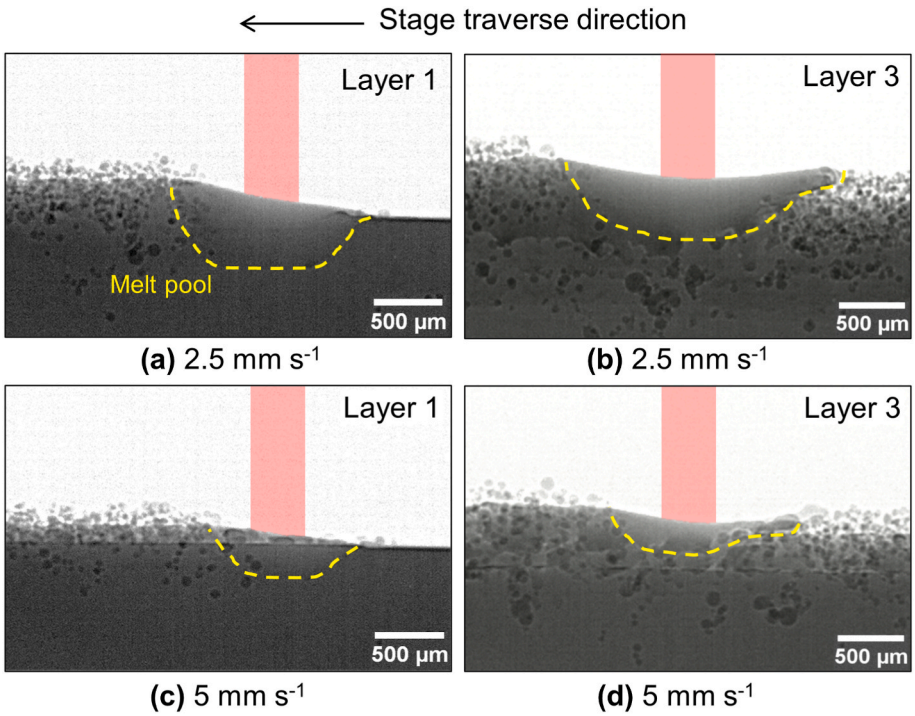

Fig. 5. Effect of traverse speed on sinter height for Ti6242 powder, with (a–b) at 2.5 mm s^{-1} and (c–d) at 5 mm s^{-1}, for $P = 200$ W and $f = 1$ g min^{-1}. The laser beam shown is in red. (a) Layer 1 deposition at 2.5 mm s^{-1} showing shallower melt pool and less powder agglomeration than Fig. 3d, and how by (b) layer 3 the melt pool is elongated. (c) Layer 1 deposition at 5 mm s^{-1} and (d) Layer 3 showing a reduction in the number of sintered particles but with reduced deposition height. See Supplementary Videos 5–8. (For interpretation of the references to colour in this figure legend, the reader is referred to the Web version of this article.)

range 700 < T < 1350 °C [23]. Liquid phase sintering occurs if a powder particle experiences enough heating to partially melt the surface and grain boundaries where segregated alloy elements lower the melting temperature, but the particle core remains solid [33,37]. The partially-molten particles wet to the surface of one another, forming a layer of sintered powder [38]. This binding mechanism is the most prevalent in the selective laser sintering process (SLS) [39,40], which typically uses a similar laser setup. Furthermore, the work undertaken has shown that the phenomenon of sintering is not confined to the alloy Ti6242 but also occurs during DED deposition of CP Ti powder, Fig. 7b.

Our hypothesis for the formation of a sintered powder layer is related to the dimensions of the powder delivery area and the melt pool surface area. If the powder focal spot is larger than the melt pool, some powder will land outside the pool and will not be incorporated (unless landing ahead of the melt pool). The powder may pass through the laser beam, and undergo heating during flight, or land on the substrate close to the melt pool, heated by the deposited track. It is known that oxides on powder surfaces can inhibit sintering [23,41], and also that titanium

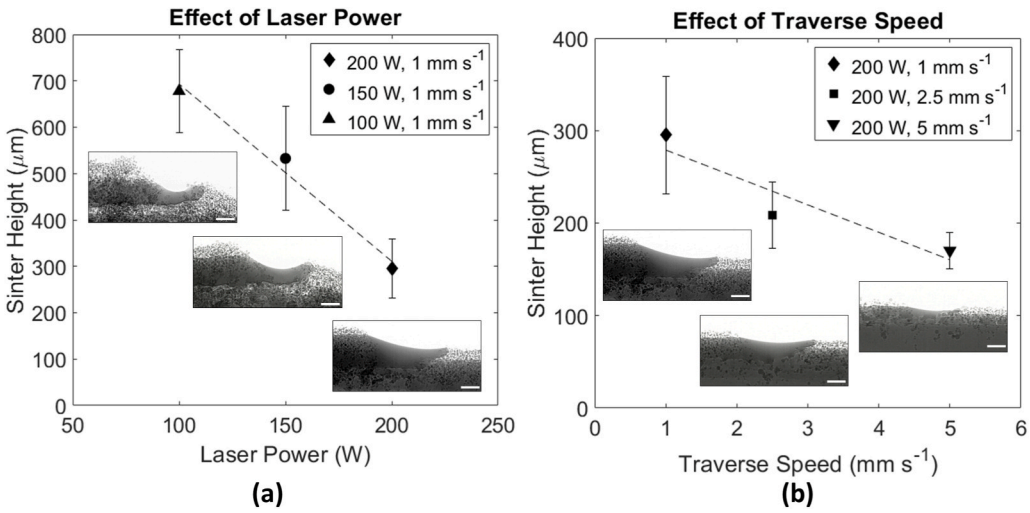

Fig. 6. Measurements of the sinter layer height, averaged across all deposited layers. (a) Changes in sinter height with laser power for constant $v = 1$ mm s^{-1}. (b) Changes in sinter height with stage traverse speed for constant $P = 200$ W. All at constant powder flowrate of $f = 1$ g min^{-1}. Error bars are calculated as the standard deviation. Inset radiographs show the variation in the measured sinter height for each condition; scale bars are 500 μm. Dotted trendlines are indicative and are not a true fit.

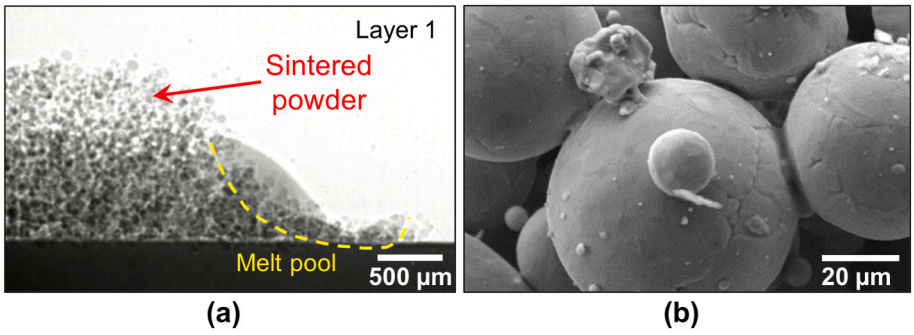

Fig. 7. (a) Radiograph image of layer 1 melting using CP Ti powder and substrate, at $P = 200$ W, $v = 2.5$ mm s^{-1}, and $f = 1$ g min^{-1}. (b) SEM image at 750× magnification of the track surface after 5 deposition layers, showing sintered powder.

dissolves its own oxide above temperatures of approximately 600 °C–700 °C [23,42]. The oxide dissolution leaves a 'clean' surface on the powder, enhancing sintering. Heated particles which land outside of the melt pool will then sinter to the track and/or other particles. Impact with the heated track could raise particle temperatures enough to induce oxide dissolution and subsequent sintering. The generation of vapour plumes from the melt pool [43] may also induce further particle heating. Heated particles can impact each other in flight, and some may sinter to one another. A recent study by Wolff et al. [14] using high-speed radiography observed two Ti–6Al–4V powder particles colliding in flight, and sintering together, perhaps as a result of surface oxide dissolution. When compared to SS316L and IN718, for example in Fig. 1, both materials form Cr-based oxides on the powder surface [21,22] which are thermodynamically stable, even at high temperatures, and hence these powders will not sinter as readily.

The physical phenomena which lead to the formation of sintered powder is discussed below, and the extent to which the present observations are relevant to a wider range of DED processing conditions is examined.

4.1. The sintered powder layer formation mechanism

For this experiment, the nozzle and approximate powder flow paths are shown schematically in Fig. 8. The powder spot diameter was measured to be 4.9 ± 0.1 mm at the working distance of 6 mm. Fig. 8 shows that the total powder footprint at the consolidation plane is significantly larger than the laser spot size, and the substrate width (400 μm, and 1 mm respectively). The percentage of deposited powder landing in the melt pool in the final deposition layer has been calculated

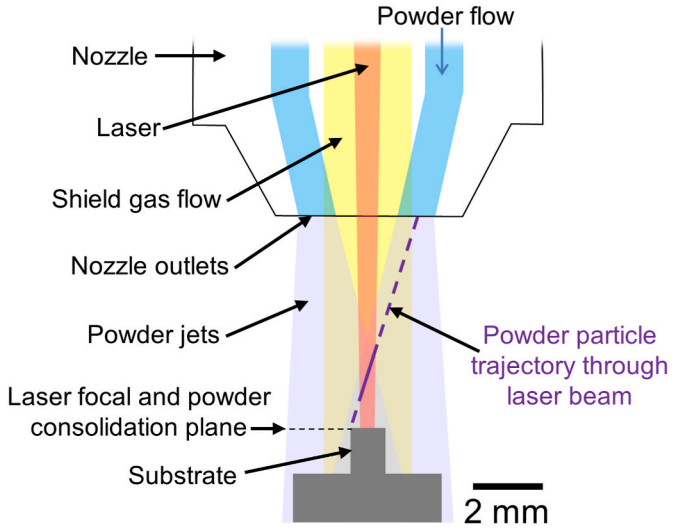

Fig. 8. 2D schematic of the DED nozzle, with approximate powder jet profiles, creating a powder spot with 4.9 ± 0.1 mm diameter at the consolidation plane. The thin wall substrate is 1 mm, and the laser spot is 400 μm. Shown by a dark purple dotted line is one possible powder particle trajectory, which passes through the centre of the laser beam but lands outside of the melt area. The solid section of line denotes the time during which the particle undergoes laser heating.

in Table 2 with details of pool measurements in Supplementary

Information. The ratio of pool area to powder spot area shows that for these experimental conditions, a maximum of *ca.* 27% of powder is landing within the melt pool. At 1 mm s^{-1}, the area ratio at 100 W is roughly half that at 200 W, meanwhile, at 100 W the sinter layer height is just over double the height at 200 W. This indicates that a critical factor in reducing sintered powder is ensuring a high powder capture efficiency. In commercial DED machines, a larger spot size is typically used alongside a higher laser power (Supplementary Table 1). The mismatch in spot size/melt pool size and the powder delivery spot size in the present work is the key criteria for the excessive sinter observed, however this work highlights the issues which may arise if processing conditions are not correct. Previous work has reported a divergence of powder delivery streams after prolonged powder feeding under a high powder feed rates, caused by erosion of the nozzle inner walls [13]. The larger powder delivery spot led to a reduction in deposit height due to a lower powder capture efficiency. This shows that DED machines can deviate from the calibrated settings with time, and unexpected process phenomena such as sinter build-up could occur. To build fine features using Ti alloys, a very focussed and accurate DED powder delivery jet would be necessary and optimising the melt pool and powder area would be key.

Previous DED models [44] assume that powder particles are either captured by the melt pool or ricochet off and are not melted, whereas this study demonstrates that an additional mechanism is present for Ti alloys in which heated particles may adhere to the track surface but do not melt. As expected from the low ratio of melt pool to powder spot, the powder capture efficiency in Table 2 is also low. However, capture efficiencies can extend across a broad range in DED depending on processing conditions. The values in Table 2 lie within the range reported in previous work using commercial DED machines, of 3–33% [45] and 5% [46]. Larger values of between 54 and 74% [47] and 38–60% have also been seen, the latter in laser cladding [2]. Powder capture efficiencies are a function of the powder focus and nozzle working distance, and previous work has shown that the track temperature affects the capture efficiency, as retained heat in the material lessens the amount of heat input required to reach melting temperature, forming a larger melt pool [48]. The formation of a sintered layer will decrease this however, as the thermal conductivity through sinter is less than bulk material.

An analysis of powder heating during deposition has been carried out, to calculate temperature increases caused by interactions with the laser beam during flight. The heating is primarily caused by the absorption of laser energy as it passes through the beam. Wen et al. [49] and Yan [50] modelled the particle heating process in DED. A calculation of the increase in temperature of individual powder particles in the carrier gas stream was carried out for the processing conditions of the present study, using Equations 4-8 in the Supplementary Information [49]. The heating was calculated for D_{10}, D_{50} and D_{90} particle sizes. Powder particles were delivered from the nozzle via four jets, at an angle of *ca.* 14°, focussed to a spot 6 mm below the outlets. The laser power was 200 W. The absorption coefficient of Ti and Ti alloys ranges from 0.3 to 0.77 [50–53], hence this range was used for this calculation. Values used are specified Supplementary Table 2.

The following assumptions have been made in this calculation:

- Powder particles travel at the same velocity as the carrier gas for the duration of their flight [12]; which is *ca.* 26 m s^{-1} for each of the four nozzle jets. Particle velocity was calculated using the volumetric flowrate, shown in Supplementary Information Equation 11. Gravity and drag forces have been considered negligible. Although previous work [44] demonstrated that the particle velocity decreases after exiting the nozzle, this effect was not calculated here. The effect of shielding gas flow on the velocity of incoming powder particles was also not accounted for.
- The carrier gas and initial particle temperature were room temperature (20 °C).
- Powder particles were considered spherical, which is appropriate for gas atomised powders [12].
- Although the powder delivery spot and laser spot are Gaussian, both were represented as a constant intensity.
- Shadowing effects of other powder particles in the stream have been considered to be negligible (*after* [12,54,55]), and particles were assumed to heat uniformly.
- Any heat gained by a powder particle would remain for their full trajectory.

Fig. 9 shows calculated temperatures of one particle travelling through the laser beam and landing outside of the melt pool on the hypothetical path labelled in Fig. 8. The plot shows that for a number of conditions the particle temperature can exceed the threshold for titanium oxide dissolution (plotted here as 700 °C [23,42]), reaching over 1300 °C for the D_{10} particle size of 50 μm, thus we hypothesise that this is causing the sintered layer. As a range of temperatures can be seen, not all particles would undergo oxide dissolution and may ricochet off the surface if not consolidated into the pool. From the SEM images of sintered powder, the particle diameter was measured for any particle exhibiting clear sintering. Across all processing conditions, the average sintered particle diameter was between 46 and 60 μm, indicating that the majority of the sinter layer was formed of particles on the low end of the particle size distribution, which supports the hypothesis of heating and oxide dissolution causing sintering. Since it has been previously reported that particle speeds decrease after exiting the nozzle [44], slower particles would remain in the laser for longer, thus reaching higher temperatures than the predicted values, and increasing the likelihood of sintering. Previous work on SS316L has shown powder particles melting and partially melting while passing through the laser beam, supporting this hypothesis that in-flight heating can be substantial [56]. Supplementary Fig. 6 shows the calculated temperatures if the particle speed was slowed to 75% of the carrier gas jet speed. It demonstrates that even for an absorption coefficient of 0.3, a 50 μm powder particle reaches *ca.* 700 °C, indicating that oxide dissolution and resultant sintering is plausible. The highest calculated temperature is *ca.* 1600 °C, which is nearing the melting temperature of titanium alloys, and may be why some particles in Fig. 2 were partially melted and fused

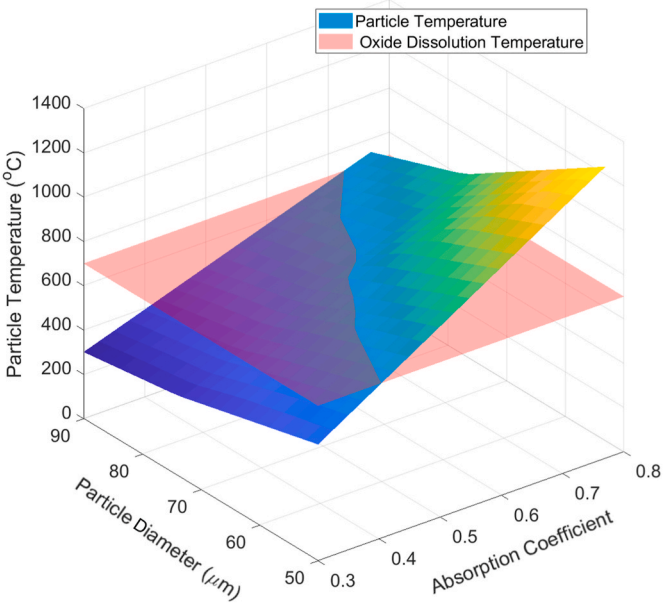

Fig. 9. Calculated temperatures of a powder particle following the path labelled in Fig. 8, for varying particle diameter (D_{10}, D_{50}, and D_{90}) and measured absorption coefficients from previous literature [51,52]. The oxide dissolution temperature is plotted as 700 °C [23,42].

together.

Substrate or track heating also takes place during deposition, and so a modified Rosenthal solution [57,58] has been used to calculate track temperatures around the melt pool. Supplementary Fig. 7a – j shows temperature contour plots with the predicted melt pool for all processing conditions, at the initial and final deposition layer. A fitting parameter has been included, which used the known melt pool length measured from the radiograph images, and fit the calculated pool geometry to this length, to predict pool depth and temperatures. The contour plots show that the temperature of the tracks behind the melt pool exceed 700 °C for all processing conditions, indicating that particles which impact the solidified track could heat and sinter upon impact. However, since the thermal conductivity through sinter is lower than solid track, any powder heating would be a secondary cause of sintering and not the predominant mechanism for the sinter layer formation.

The Rosenthal solution predicted deeper melt pools than measured from radiograph images; an average of 45% deeper for layer 1 and 121% deeper for the final deposition layer across all conditions. The large mismatch between measured and predicted depths in the final layer may be a result of the sinter layer: as can be seen in Figs. 4 and 5, the sinter causes melt pools to become elongated and shallower. It is thought that this is due to a change in pool wetting, onto powder as opposed to previously deposited track. The sintered powder almost acts like a pre-deposited powder layer in LPBF, and the melt pool must percolate through and melt the layer of powder in addition to incoming powder to ensure sufficient layer cohesion. Previous work on melt pool and powder interactions has shown low wettability of powder particles, related to oxides on powder surfaces [59]; this effect may further alter the wetting of the pool. The elongation of melt pools could increase powder capture; however, the subsequent shallowing of the pools decreases the inter-layer cohesion and can lead to lack of fusion porosity. The thermal gradients in the melt pool are also likely to be affected by the sinter layer, as heat transfer through sintered powder will be different than solid track. This could contribute to the melt pool shape change compared to other alloys, as seen in Fig. 1.

The differing melt pool shapes have been referenced in previous works [20], describing it as 'saddle-shaped' as a result of sintered powder. The μCT cross sections in Fig. 3 show the inverted melt pool shape, and an increase in track width as layer number increases for all conditions. Previous studies have also revealed a similar 'saddle' shape of deposited Ti–6Al–4V [60,61] and Ti6242 [5], and the agglomeration of powder Ti–6Al–4V particles on track surfaces [26]. The saddle shaped melt pool was attributed to Marangoni flow in the melt pool, in which material flows downwards at pool edges and is pushed upwards in the centre [26]. It is speculated that sinter layer could contribute to this saddle shaped pool if the melt pool spreads over the surface of the sinter. This could be exacerbated each time a new layer is deposited, as the melt pool could penetrate through the sinter layer, but also flow through the sinter down the sides of the track, rather than creating a deep hemispherical melt pool as expected. This effect would likely be reduced in a hatched melting strategy, as sinter on the sides of a track could be remelted and incorporated into the pool. The saddle effect which causes the melt pool width to increase with each layer could potentially be advantageous, if a need for such geometries arose.

Fig. 10 and Supplementary Video 15 show a Ti6242 sample in which the track was built under atmospheric conditions, instead of an argon purged chamber. The shield and carrier gas remained at the same flowrates; identical conditions were used for both builds, with the exception of the atmosphere. Although there is internal porosity being carried in the melt pool and significant cracking at the ends of the track during solidification due to increased oxygen content, one key observation is that there is no powder sintering on the track surface or during melting. A hypothesis for this is that in an atmosphere containing oxygen, the powder will still be heated if passing through the laser, and the oxide dissolution will take place, however, surrounding oxygen is present to continually replenish the oxide layer, meaning that powder

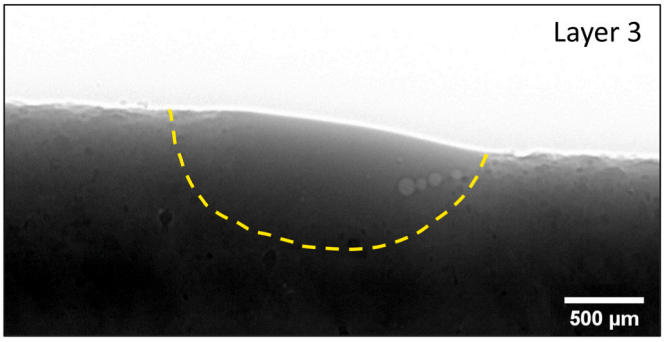

Fig. 10. Oxidised Ti6242 sample at $P = 200$ W, $v = 1$ mm s^{-1}. The oxygenated atmosphere introduces pores into the melt pool, but most importantly reveals that no sintered powder is present on previous layers or surrounding the melt pool. The melt pool shape resembles the SS316L sample more closely with a convex melt pool surface. See Supplementary Video 15.

particles cannot sinter, as oxides inhibit sintering in metal powders [23,41]. All incoming powder is either incorporated into the pool and melted or ricochets off the track surface, matching our hypothesis. The melt pool shape in this condition is convex (similar to SS316L and IN718), rather than concave as observed in all other Ti conditions. Any resultant changes to the formation of a vapour plume or subsequent effect on powder sintering are considered negligible. A computational model of vapour plumes by Chen and Yan considered a convection mode situation [62], in which the velocity of the induced gas was *ca.* 0.4 m s^{-1}, which is over an order of magnitude smaller than 26 m s^{-1} gas flow exiting the nozzle in this study.

4.2. Relationship to processing conditions

The difference between titanium alloys and other materials is evident from Fig. 1. The concave as opposed to the convex-shaped melt pool and change in wetting at the leading edge of the pool is a direct result of powder sintering during deposition. The sintered particles in Fig. 2 suggest varying degrees of powder heating in flight between the nozzle and melt pool area, as although some particles had partially melted, the majority of powder particles were sintered as demonstrated in Fig. 2c.

The difference in the height of the sinter layer on the track surface was most noticeable when varying laser power. From the radiograph images in Figs. 4 and 5 and measurements in Fig. 6, it is clear that laser power has the largest influence on the melt pool size, and thus strongly impacts the sinter layer height. Fig. 4 shows that the melt pool created at 200 W is significantly larger than the laser spot size, and the melt pool covers more of the powder spot (*ca.* 27% overlap). For the 100 W condition, the pool is significantly smaller, and so the same amount of powder is flowing into the melt area, but a larger amount will land outside of the melt pool.

Increased traverse speed reduced the energy density and melt pool size, however, the reduced sinter layer height with increasing speed seen in Fig. 6 is a result of less powder being delivered to the laser spot during melting. The effect of increasing traverse speed is essentially analogous to decreasing powder feed rate for a constant speed. Thinner deposition layers were also caused by this reduction in available material, as well as smaller melt pools due to lower overall energy density.

To consider possible conditions which could reduce the sinter layer, the trendlines in Fig. 6 were extrapolated to the point at which sinter height was zero. Assuming a continuous linear relationship, this revealed that a laser power of *ca.* 280 W or higher could sufficiently decrease the sintered layer, likely by causing a larger melt pool and increasing the powder capture efficiency. For traverse speed, the extrapolation indicated that at 200 W, a speed of *ca.* 10.5 mm s^{-1} or higher would be necessary to reduce the sinter height to zero. However, such speeds would substantially reduce the deposition height, as only

half as much powder as the 5 mm s^{-1} condition would be fed into the system and available for melting, thus, increasing traverse speed would not be a suitable method of reducing powder sintering. Furthermore, the relationship between processing parameters and sinter height is likely not strictly linear, and increasing laser power or traverse speed could make the sinter negligible but not eliminate it entirely.

5. Conclusions

This work has provided a parametric study of a previously observed Ti alloy powder sintering phenomenon in DED, and has utilised *in situ* radiography to quantify the effects of different processing conditions on sinter build-up.

Sintering was present under all processing conditions investigated, but the thickness of the sinter layer varied. Increasing laser power, thereby creating a larger melt pool, decreased the sinter layer thickness on the surface of deposits. Increasing traverse speed (akin to reducing powder feed rate) also reduced the sinter, but was at a compromise of reduced deposition height.

A high powder capture efficiency by minimising any mismatch between the pool area and the powder delivery area is necessary to mitigate sinter formation in Ti alloys. Unoptimised processing conditions such as a very high powder feed rate could induce sintering if the incoming powder exceeds the melt pool capture ability.

Sinter is caused by powder heating, primarily via laser beam attenuation during flight. Particle heating calculations confirmed that Ti6242 powder particles can reasonably exceed 700 °C, resulting in surface oxide dissolution and subsequent sintering, under the processing conditions explored in this work.

The build-up of sintered powder layers can cause lack of fusion defects between layers, which were most prevalent in low laser power conditions, and is a feature to be aware of in commercial processing.

Author statement

Lorna Sinclair: Conceptualisation, Methodology, Validation, Formal analysis, Investigation, Data curation, Writing – original draft, Writing – review & editing, Visualization. Yunhui Chen: Conceptualisation, Investigation. Samuel J. Clark: Software, Formal analysis, Investigation. Sebastian Marussi: Investigation. Saurabh Shah: Investigation. Oxana V. Magdysyuk: Resources. Robert Atwood: Resources. Gavin J. Baxter: Writing – review & editing, Supervision. Martyn Jones: Writing – review & editing, Supervision. Graham McCartney: Writing – review & editing. Chu Lun Alex Leung: Investigation, Writing – review & editing. Peter D. Lee: Conceptualisation, Writing – review & editing, Project administration, Funding acquisition.

Declaration of competing interest

The authors declare that they have no known competing financial interests or personal relationships that could have appeared to influence the work reported in this paper.

Acknowledgements

The authors acknowledge financial support from the EPSRC MAPP Future Manufacturing Hub (EP/P006566/1, www.mapp.ac.uk); The Royal Academy of Engineering (CiET1819/10); Rolls-Royce Plc. Through the Horizon 2020 Clean Sky 2 WP5.8.1 programmes (YC) and LS's Industrial Case studentship. We acknowledge the Research Complex at Harwell for use of facilities and thank Diamond Light Source Ltd. For providing the beamtime at beamline I12 (MT20096-5). A special thanks to other PhD students and team members for their assistance during the beamtime.

Appendix A. Supplementary data

Supplementary data to this article can be found online at https://doi.org/10.1016/j.ijmachtools.2022.103887.

References

[1] S.M. Thompson, L. Bian, N. Shamsaei, A. Yadollahi, An overview of Direct Laser Deposition for additive manufacturing; Part I: transport phenomena, modeling and diagnostics, Addit. Manuf. 8 (2015) 36–62, https://doi.org/10.1016/j.addma.2015.07.001.

[2] A. Frenk, M. Vandyoussefi, J.D. Wagniere, A. Zryd, W. Kurz, Analysis of the laser-cladding process for stellite on steel, Metall. Mater. Trans. B Process Metall. Mater. Process. Sci. 28 (1997) 501–508, https://doi.org/10.1007/s11663-997-0117-0.

[3] S. Nam, H. Cho, C. Kim, Y.M. Kim, Effect of process parameters on deposition properties of functionally graded STS 316/Fe manufactured by laser direct metal deposition, Metals 8 (2018), https://doi.org/10.3390/met8080607.

[4] B.E. Carroll, R.A. Otis, J.P. Borgonia, J.O. Suh, R.P. Dillon, A.A. Shapiro, D. C. Hofmann, Z.K. Liu, A.M. Beese, Functionally graded material of 304L stainless steel and inconel 625 fabricated by directed energy deposition: characterization and thermodynamic modeling, Acta Mater. 108 (2016) 46–54, https://doi.org/10.1016/j.actamat.2016.02.019.

[5] K.-H. Richter, S. Orban, S. Nowotny, Laser cladding of the titanium alloy TI6242 to restore damaged blades, in: 3rd Int. Congr. Appl. Lasers Electro-Optics, 2004, https://doi.org/10.2351/1.5060222.

[6] A.J. Pinkerton, W. Wang, L. Li, Component repair using laser direct metal deposition, Proc. Inst. Mech. Eng. Part B J. Eng. Manuf. 222 (2008) 827–836, https://doi.org/10.1243/09544054JEM1008.

[7] A. Bobel, L.G. Hector, I. Chelladurai, A.K. Sachdev, T. Brown, W.A. Poling, R. Kubic, B. Gould, C. Zhao, N. Parab, A. Greco, T. Sun, In situ synchrotron X-ray imaging of 4140 steel laser powder bed fusion, Materialia 6 (2019) 100306, https://doi.org/10.1016/J.MTLA.2019.100306.

[8] G.K.L. Ng, A.E.W. Jarfors, G. Bi, H.Y. Zheng, Porosity formation and gas bubble retention in laser metal deposition, Appl. Phys. Mater. Sci. Process 97 (2009) 641–649, https://doi.org/10.1007/s00339-009-5266-3.

[9] M. Fujishima, Y. Oda, R. Ashida, K. Takezawa, M. Kondo, Study on factors for pores and cladding shape in the deposition processes of Inconel 625 by the directed energy deposition (DED) method, CIRP J. Manuf. Sci. Technol. 19 (2017) 200–204, https://doi.org/10.1016/j.cirpj.2017.04.003.

[10] A.J. Pinkerton, L. Li, The significance of deposition point standoff variations in multiple-layer coaxial laser cladding (coaxial cladding standoff effects), Int. J. Mach. Tool Manufact. 44 (2004) 573–584, https://doi.org/10.1016/j.ijmachtools.2004.01.001.

[11] J. hua Wang, F. zhu Han, S. fan Chen, W. sheng Ying, A novel model of laser energy attenuation by powder particles for laser solid forming, Int. J. Mach. Tool Manufact. 145 (2019) 103440, https://doi.org/10.1016/j.ijmachtools.2019.103440.

[12] A.J. Pinkerton, An analytical model of beam attenuation and powder heating during coaxial laser direct metal deposition, J. Phys. D Appl. Phys. 40 (2007) 7323–7334, https://doi.org/10.1088/0022-3727/40/23/012.

[13] H. Tan, C. Zhang, W. Fan, F. Zhang, X. Lin, J. Chen, W. Huang, Dynamic evolution of powder stream convergence with powder feeding durations in direct energy deposition, Int. J. Mach. Tool Manufact. 157 (2020) 103606, https://doi.org/10.1016/j.ijmachtools.2020.103606.

[14] S.J. Wolff, H. Wu, N. Parab, C. Zhao, K.F. Ehmann, T. Sun, J. Cao, In-situ high-speed X-ray imaging of piezo-driven directed energy deposition additive manufacturing, Sci. Rep. 9 (2019) 1–14, https://doi.org/10.1038/s41598-018-36678-5.

[15] S. Webster, S. Wolff, J. Bennett, T. Sun, J. Cao, K. Ehmann, porosity formation and meltpool geometry analysis using high-speed , in situ imaging of directed energy deposition, Microsc. Microanal. 25 (2019) 2556–2557, https://doi.org/10.1017/S1431927619013515.

[16] A. Lindenmeyer, S. Webster, M.F. Zaeh, K.F. Ehmann, J. Cao, Template-bayesian approach for the evaluation of melt pool shape and dimension of a DED-process from in-situ X-ray images, CIRP Ann 70 (2021) 183–186, https://doi.org/10.1016/j.cirp.2021.03.011.

[17] S.J. Wolff, S. Webster, N.D. Parab, B. Aronson, B. Gould, A. Greco, T. Sun, In-situ observations of directed energy deposition additive manufacturing using high-speed X-ray imaging, JOM (J. Occup. Med.) 73 (2021) 189–200, https://doi.org/10.1007/s11837-020-04469-x.

[18] Y. Chen, S.J. Clark, Y. Huang, L. Sinclair, C. Lun Alex Leung, S. Marussi, T. Connolley, O.V. Magdysyuk, R.C. Atwood, G.J. Baxter, M.A. Jones, I. Todd, P. D. Lee, In situ X-ray quantification of melt pool behaviour during directed energy deposition additive manufacturing of stainless steel, Mater. Lett. 286 (2021) 129205, https://doi.org/10.1016/j.matlet.2020.129205.

[19] Y. Chen, S.J. Clark, D.M. Collins, S. Marussi, S.A. Hunt, D.M. Fenech, T. Connolley, R.C. Atwood, O.V. Magdysyuk, G.J. Baxter, M.A. Jones, C.L.A. Leung, P.D. Lee, Correlative synchrotron X-ray imaging and diffraction of directed energy deposition additive manufacturing, Acta Mater. 209 (2021) 116777, https://doi.org/10.2139/ssrn.3702822.

[20] Y. Chen, S.J. Clark, L. Sinclair, C.L.A. Leung, S. Marussi, T. Connolley, R. C. Atwood, G.J. Baxter, M.A. Jones, I. Todd, P.D. Lee, Synchrotron X-ray imaging of directed energy deposition additive manufacturing of titanium alloy Ti-6242, Addit. Manuf. 41 (2021) 101969.

[21] J. Yan, Y. Zhou, R. Gu, X. Zhang, W.M. Quach, M. Yan, A comprehensive study of steel powders (316L, H13, P20 and 18Ni300) for their selective laser melting additive manufacturing, Metals 9 (2019), https://doi.org/10.3390/met9010086.
[22] H. Yu, S. Hayashi, K. Kakehi, Y.L. Kuo, Study of formed oxides in IN718 alloy during the fabrication by selective laser melting and electron beam melting, Metals 9 (2019), https://doi.org/10.3390/met9010019.
[23] M. Qian, G.B. Schaffer, C.J. Bettles, Sintering of titanium and its alloys, Sinter. Adv. Mater. (2010) 324–355, https://doi.org/10.1533/9781845699949.3.324.
[24] B. Zheng, J.C. Haley, N. Yang, J. Yee, K.W. Terrassa, Y. Zhou, E.J. Lavernia, J. M. Schoenung, On the evolution of microstructure and defect control in 316L SS components fabricated via directed energy deposition, Mater. Sci. Eng. 764 (2019), https://doi.org/10.1016/j.msea.2019.138243.
[25] W.U.H. Syed, A.J. Pinkerton, L. Li, A comparative study of wire feeding and powder feeding in direct diode laser deposition for rapid prototyping, Appl. Surf. Sci. 247 (2005) 268–276, https://doi.org/10.1016/j.apsusc.2005.01.138.
[26] M. Gharbi, P. Peyre, C. Gorny, M. Carin, S. Morville, P. Le Masson, D. Carron, R. Fabbro, Influence of various process conditions on surface finishes induced by the direct metal deposition laser technique on a Ti-6Al-4V alloy, J. Mater. Process. Technol. 213 (2013) 791–800, https://doi.org/10.1016/j.jmatprotec.2012.11.015.
[27] C.L.A. Leung, S. Marussi, R.C. Atwood, P.D. Lee, M. Towrie, P.J. Withers, In situ X-ray imaging of defect and molten pool dynamics in laser additive manufacturing, Nat. Commun. 9 (2018) 1–9, https://doi.org/10.1038/s41467-018-03734-7.
[28] M. Drakopoulos, T. Connolley, C. Reinhard, R. Atwood, O. Magdysyuk, N. Vo, M. Hart, L. Connor, B. Humphreys, G. Howell, S. Davies, T. Hill, G. Wilkin, U. Pedersen, A. Foster, N. De Maio, M. Basham, F. Yuan, K. Wanelik, I12: the Joint engineering, environment and processing (JEEP) beamline at Diamond Light source, J. Synchrotron Radiat. 22 (2015) 828–838, https://doi.org/10.1107/S1600577515003513.
[29] G.N. Ramachandran, A.V. Lakshminarayanan, Three-dimensional reconstruction from radiographs and electron micrographs : application of convolutions instead of fourier transforms, in: Proc. Natl. Acad. Sci. U. S. A., 1971, pp. 2236–2240.
[30] C.L.A. Leung, S. Marussi, M. Towrie, J. del Val Garcia, R.C. Atwood, A.J. Bodey, J. R. Jones, P.J. Withers, P.D. Lee, Laser-matter interactions in additive manufacturing of stainless steel SS316L and 13-93 bioactive glass revealed by in situ X-ray imaging, Addit. Manuf. 24 (2018) 647–657, https://doi.org/10.1016/j.addma.2018.08.025.
[31] S. Yue, P.D. Lee, G. Poologasundarampillai, J.R. Jones, Evaluation of 3-D bioactive glass scaffolds dissolution in a perfusion flow system with X-ray microtomography, Acta Biomater. 7 (2011) 2637–2643, https://doi.org/10.1016/j.actbio.2011.02.009.
[32] J. Schindelin, I. Arganda-Carreras, E. Frise, V. Kaynig, M. Longair, T. Pietzsch, S. Preibisch, C. Rueden, S. Saalfeld, B. Schmid, J.Y. Tinevez, D.J. White, V. Hartenstein, K. Eliceiri, P. Tomancak, A. Cardona, Fiji: an open-source platform for biological-image analysis, Nat. Methods 9 (2012) 676–682, https://doi.org/10.1038/nmeth.2019.
[33] R.M. German, Sintering from Empirical Observations to Scientific Principles, Elsevier Science & Technology, Oxford, 2014, https://doi.org/10.1016/B978-0-12-401682-8.00017-3.
[34] T. Schmidt, F. Gärtner, H. Assadi, H. Kreye, Development of a generalized parameter window for cold spray deposition, Acta Mater. 54 (2006) 729–742, https://doi.org/10.1016/j.actamat.2005.10.005.
[35] D. Goldbaum, J.M. Shockley, R.R. Chromik, A. Rezaeian, S. Yue, J.G. Legoux, E. Irissou, The effect of deposition conditions on adhesion strength of Ti and Ti6Al4V cold spray splats, J. Therm. Spray Technol. 21 (2012) 288–303, https://doi.org/10.1007/s11666-011-9720-3.
[36] R.M. German, P. Suri, S. Jin Park, Review: liquid phase sintering, J. Mater. Sci. (2009) 1–39, https://doi.org/10.1007/s10853-008-3008-0.
[37] J. Kruth, J. Van Vaerenbergh, Binding mechanisms in selective laser sintering and selective laser melting, Rapid Prototyp. J. 11 (2005) 26–36.
[38] L. Edwards, M. Endean (Eds.), Manufacturing with Materials, second ed., Open University, 1990.
[39] S. Kumar, Selective laser sintering: a qualitative and objective approach, J. Miner. Met. Mater. Soc. 55 (2003) 43–47.
[40] P. Fischer, M. Locher, V. Romano, H.P. Weber, S. Kolossov, R. Glardon, Temperature measurements during selective laser sintering of titanium powder, 44, 2004, pp. 1293–1296, https://doi.org/10.1016/j.ijmachtools.2004.04.019.
[41] Z.Z. Fang, J.D. Paramore, P. Sun, K.S.R. Chandran, Y. Zhang, Y. Xia, F. Cao, M. Koopman, M. Free, Powder metallurgy of titanium–past, present, and future, Int. Mater. Rev. 63 (2018) 407–459, https://doi.org/10.1080/09506608.2017.1366003.
[42] Y.F. Yang, M. Qian, Fundamental understanding of the dissolution of oxide film on Ti powder and the unique scavenging feature by LaB6, Metall. Mater. Trans. A Phys. Metall. Mater. Sci. 49 (2018) 1–6, https://doi.org/10.1007/s11661-017-4366-5.
[43] P. Bidare, I. Bitharas, R.M. Ward, M.M. Attallah, A.J. Moore, Fluid and particle dynamics in laser powder bed fusion, Acta Mater. 142 (2018) 107–120, https://doi.org/10.1016/j.actamat.2017.09.051.
[44] S. Zekovic, R. Dwivedi, R. Kovacevic, Numerical simulation and experimental investigation of gas-powder flow from radially symmetrical nozzles in laser-based direct metal deposition, Int. J. Mach. Tool Manufact. 47 (2007) 112–123, https://doi.org/10.1016/j.ijmachtools.2006.02.004.
[45] K.L. Terrassa, J.C. Haley, B.E. MacDonald, J.M. Schoenung, Reuse of powder feedstock for directed energy deposition, Powder Technol. 338 (2018) 819–829, https://doi.org/10.1016/j.powtec.2018.07.065.
[46] P.A. Carroll, A.J. Pinkerton, J. Allen, W.U.H. Syed, H.K. Sezer, P. Brown, G. Ng, R. Scudamore, L. Li, The effect of powder recycling in direct metal laser deposition on powder and manufactured part characteristics, in: Proc. AVT-139 Spec. Meet. Cost Eff. Manuf. Via Net Shape Process. NATO Res. Technol. Organ., 2006, pp. 1–8. http://eprints.lancs.ac.uk/59645/.
[47] Y. Kakinuma, M. Mori, Y. Oda, T. Mori, M. Kashihara, A. Hansel, M. Fujishima, Influence of metal powder characteristics on product quality with directed energy deposition of Inconel 625, CIRP Ann. - Manuf. Technol. 65 (2016) 209–212, https://doi.org/10.1016/j.cirp.2016.04.058.
[48] J.C. Haley, B. Zheng, U.S. Bertoli, A.D. Dupuy, J.M. Schoenung, E.J. Lavernia, Working distance passive stability in laser directed energy deposition additive manufacturing, Mater. Des. 161 (2019) 86–94, https://doi.org/10.1016/j.matdes.2018.11.021.
[49] S.Y. Wen, Y.C. Shin, J.Y. Murthy, P.E. Sojka, Modeling of coaxial powder flow for the laser direct deposition process, Int. J. Heat Mass Tran. 52 (2009) 5867–5877, https://doi.org/10.1016/j.ijheatmasstransfer.2009.07.018.
[50] J. Yan, Optimal Design of Process Parameters during Laser Direct Metal Deposition of Multi-Material Parts, Clemson University, 2016. http://tigerprints.clemson.edu/all_dissertations/1813.
[51] F. Lia, J. Park, J. Tressler, R. Martukanitz, Partitioning of laser energy during directed energy deposition, Addit. Manuf. 18 (2017) 31–39, https://doi.org/10.1016/j.addma.2017.08.012.
[52] N.K. Tolochko, T. Laoiu, Y.V. Khlopkov, S.E. Mozzharov, V.I. Titov, M.B. Ignatiev, Absorptance of powder materials suitable for laser sintering 6 (2000) 155–160.
[53] R. Rai, J.W. Elmer, T.A. Palmer, T. Debroy, Heat transfer and fluid flow during keyhole mode laser welding of tantalum, Ti-6Al-4V, 304L stainless steel and vanadium, J. Phys. D Appl. Phys. 40 (2007) 5753–5766, https://doi.org/10.1088/0022-3727/40/18/037.
[54] J. Liu, L. Li, Y. Zhang, X. Xie, Attenuation of laser power of a focused Gaussian beam during interaction between a laser and powder in coaxial laser cladding 38 (2005) 1546–1550, https://doi.org/10.1088/0022-3727/38/10/008.
[55] J. Lin, Temperature analysis of the powder streams in coaxial laser cladding, Opt Laser. Technol. 31 (2000) 565–570.
[56] J.C. Haley, J.M. Schoenung, E.J. Lavernia, Observations of particle-melt pool impact events in directed energy deposition, Addit. Manuf. 22 (2018) 368–374, https://doi.org/10.1016/j.addma.2018.04.028.
[57] D. Rosenthal, The Theory of Moving Sources of Heat and its Application to Metal Treatments.Pdf, 1946, pp. 849–866.
[58] S. Bontha, N.W. Klingbeil, P.A. Kobryn, H.L. Fraser, Thermal process maps for predicting solidification microstructure in laser fabrication of thin-wall structures, J. Mater. Process. Technol. 178 (2006) 135–142, https://doi.org/10.1016/j.jmatprotec.2006.03.155.
[59] J.C. Haley, J.M. Schoenung, E.J. Lavernia, Modelling particle impact on the melt pool and wettability effects in laser directed energy deposition additive manufacturing, Mater. Sci. Eng. 761 (2019) 138052, https://doi.org/10.1016/j.msea.2019.138052.
[60] M.N. Ahsan, R. Bradley, A.J. Pinkerton, Microcomputed tomography analysis of intralayer porosity generation in laser direct metal deposition and its causes, J. Laser Appl. 23 (2011), 022009, https://doi.org/10.2351/1.3582311.
[61] M. Gharbi, P. Peyre, C. Gorny, M. Carin, S. Morville, P. Le Masson, D. Carron, R. Fabbro, Influence of a pulsed laser regime on surface finish induced by the direct metal deposition process on a Ti64 alloy, J. Mater. Process. Technol. 214 (2014) 485–495, https://doi.org/10.1016/j.jmatprotec.2013.10.004.
[62] H. Chen, W. Yan, Spattering and denudation in laser powder bed fusion process: multiphase flow modelling, Acta Mater. 196 (2020) 154–167, https://doi.org/10.1016/j.actamat.2020.06.033.